

A complete ^{12}CO 2–1 map of M51 with HERA: II. Total gas surface densities and gravitational stability

M. Hitschfeld¹, C. Kramer^{1,2}, K.F. Schuster³, S. Garcia-Burillo⁴, and J. Stutzki¹

¹ KOSMA, I. Physikalisches Institut, Universität zu Köln, Zùlpicher StraÙe 77, 50937 Köln, Germany

² IRAM, Avenida Divina Pastora 7, Núcleo Central, E-18012 Granada, Spain

³ IRAM, 300 Rue de la Piscine, F-38406 S^t Martin d'Hères, France

⁴ Observatorio de Madrid, Alfonso XII, 3, 28014 Madrid, Spain

Received / Accepted

ABSTRACT

Context. To date the onset of large-scale star formation in galaxies and its link to gravitational stability of the galactic disk have not been fully understood. The nearby face-on spiral galaxy M51 is an ideal target for studying this subject.

Aims. This paper combines CO, dust, H I, and stellar maps of M51 and its companion galaxy to study the H₂/H I transition, the gas-to-dust ratios, and the stability of the disk against gravitational collapse.

Methods. We combine maps of the molecular gas using ^{12}CO 2–1 map HERA/IRAM-30m data and H I VLA data to study the total gas surface density and the phase transition of atomic to molecular gas. The total gas surface density is compared to the dust surface density from 850 μm SCUBA data. Taking into account the velocity dispersions of the molecular and atomic gas, and the stellar surface densities derived from the 2MASS *K*-band survey, we derive the total Toomre Q parameter of the disk.

Results. The gas surface density Σ_{gas} in the spiral arms is $\sim 2 - 3$ higher compared to that of the interarm regions. The ratio of molecular to atomic surface density shows a nearly power-law dependence on the hydrostatic pressure P_{hydro} . The Σ_{gas} distribution in M51 shows an underlying exponential distribution with a scale length of $h_{\text{gas}} = 7.6$ kpc representing 55% of the total gas mass, comparable to the properties of the exponential dust disk. In contrast to the velocity widths observed in H I, the CO velocity dispersion shows enhanced line widths in the spiral arms compared to the interarm regions. The contribution of the stellar component in the Toomre Q-parameter analysis is significant and lowers the combined Q-parameter Q_{tot} by up to 70% towards the threshold for gravitational instability. The value of Q_{tot} varies from 1.5-3 in radial averages. A map of Q_{tot} shows values around 1 on the spiral arms indicating self-regulation at play.

Key words. Keywords should be given

1. Introduction

To understand the evolution and appearance of galaxies it is crucial to study the interplay between stars and the interstellar gas and dust. Stars are made within the dense and cold interiors of molecular clouds. It is generally believed that molecular clouds form from the densest regions of more widely distributed, diffuse atomic clouds. During their lifetimes, stars seed the gas with heavy elements, energy, and momentum, all of which strongly affects their parental environment, the subsequent formation of new stars, and their host galaxy. The photo-destruction of molecular clouds leads to their dispersal and the formation of diffuse atomic clouds, thereby recycling the material. The processes governing the phase transition from

the cold neutral medium to dense, molecular gas, and back again, are however still unclear (Rosolowsky et al. 2007; Knapen et al. 2006; Heitsch et al. 2008). Studies combining maps of CO, the traditional tracer of molecular gas, H I, and the cold dust will form the basis for any understanding of their interrelation. The spatial distribution of the various galactic components is best studied in nearby face-on galaxies, like M51, which lies at a distance of 8.4 Mpc (Feldmeier et al. 1997).

Two empirical laws describe star formation in galaxies. First, stars are observed to only form efficiently above a critical gas surface density that appears to be determined by the Toomre (Toomre 1964) criterion for gravitational stability. This star formation threshold has been observed in many galaxies (e.g. Martin & Kennicutt 2001). Note, however the exceptions discussed e.g. by Wong & Blitz (2002). Second, a tight relation has been found between

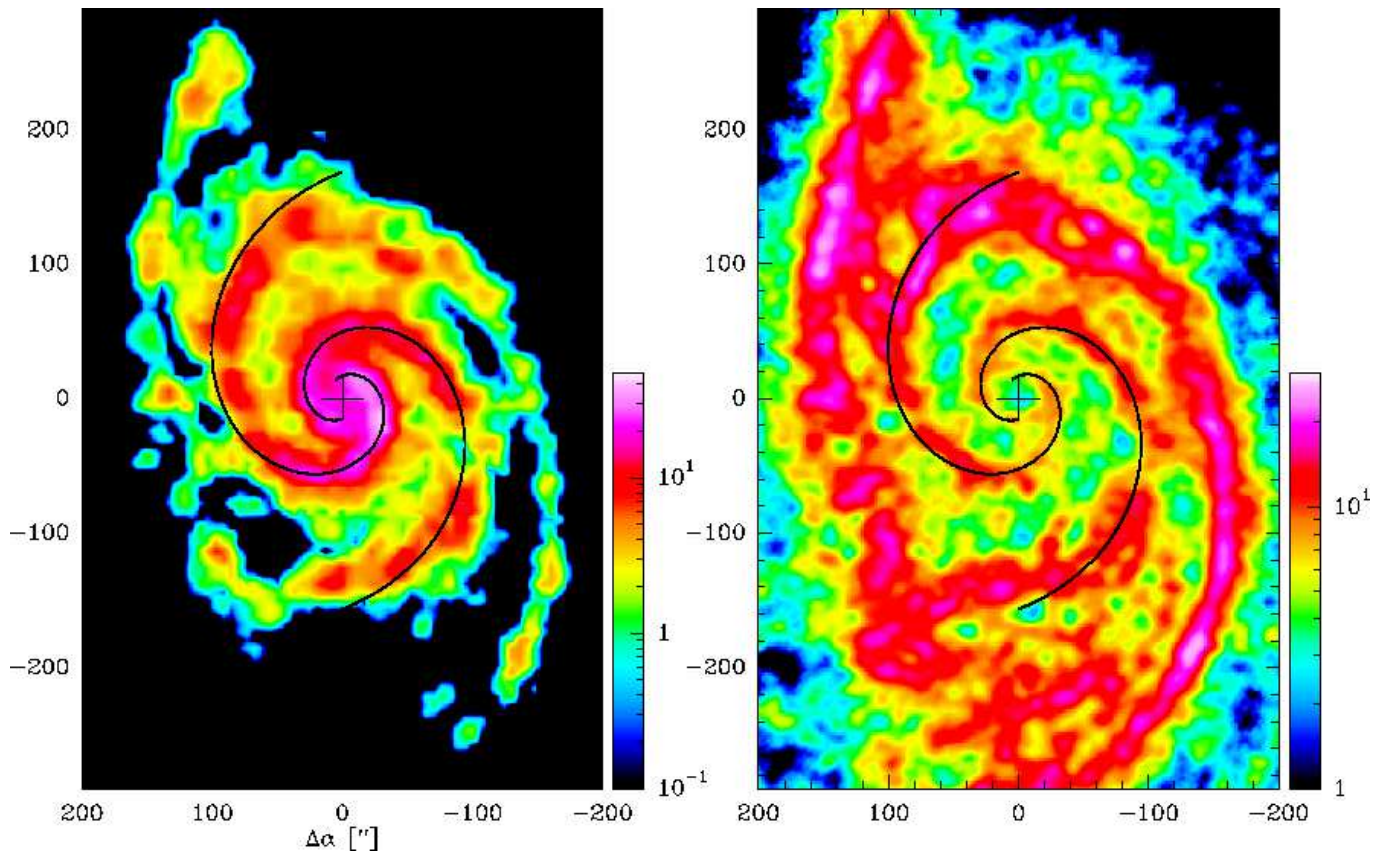


Fig. 1. Left: Map of integrated CO 2–1 intensities on the antenna temperature scale in K km s^{-1} at $11''$ resolution (cf. Paper I). A logarithmic spiral is shown in all Figures of M51 to guide the eye. **Right:** Map of HI column densities (Walter et al. 2008) in units of 10^{20} cm^{-2} at a resolution of $\sim 6''$.

the star formation rate and the surface density of the total gas, i.e. the molecular and atomic gas, the Schmidt law. In this paper, we will focus on the Toomre criterion.

In its original version it considers a dynamical stability analysis of a thin, gaseous, differentially rotating, single-component disk against axisymmetric gravitational perturbations. Observational studies of the Toomre threshold have usually assumed a constant velocity dispersion of the gas, while Schaye (2004) questions this assumption, arguing that the drop of velocity dispersion associated with the transition from the warm to a cold phase of the interstellar medium causes the disk to become gravitationally unstable. In addition, recent studies have shown that the stellar component contributes significantly to the gravitational stability and cannot be neglected (Boissier et al. 2003; Yang et al. 2007).

In Schuster et al. (2007, hereafter Paper I), we combined new CO 2–1 data of M51 obtained at the IRAM-30m telescope using HERA, with HI, and radio continuum data from the literature to discuss radial profiles of the molecular and atomic gas mass surface densities and star formation rates, averaged over azimuth as a function of radius in the disk of M51. In the following, we will simply speak of radial averages.

In the present paper, we combine the CO 2–1 data with HI VLA data from the THINGS survey

(Walter et al. 2005, 2008), $850 \mu\text{m}$ SCUBA dust continuum data (Meijerink et al. 2005), and a *K*-Band 2MASS image. We use the CO and HI data to derive maps of the mass surface densities of the molecular and atomic gas, and maps of their velocity dispersions. Maps of the total gas and of the ratio of molecular to atomic gas are then discussed. We separate the total gas mass surface density map into an underlying exponential disk and the spiral arm structure. The results are then compared with the dusty exponential disk found by Meijerink et al. (2005) in their SCUBA map of M51. This allows us to study the variation of the gas-to-dust ratios in the disk and in the arms.

In preparation for the Toomre analysis, we discuss the velocity dispersions of the molecular and atomic gas. Combining the data of the molecular and atomic gas with the map of stellar mass surface density derived from the 2MASS data, we then present the radial average and a map of the total Toomre Q parameter describing the gravitational stability of the disk.

2. Observations and Data

Observations of the ^{12}CO 2–1 emission from M51 were conducted with the IRAM 30m telescope in February

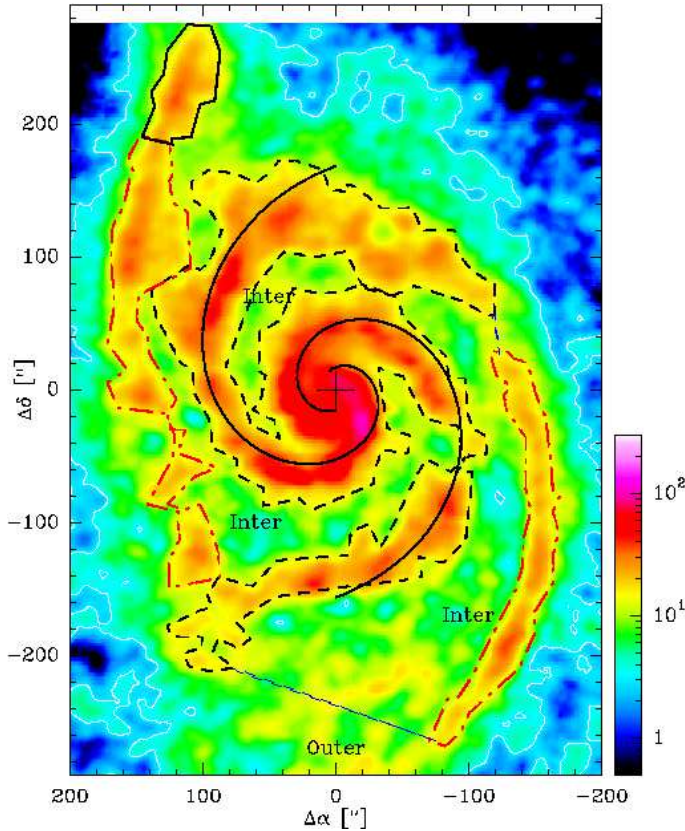


Fig. 2. Map of the total gas mass surface density Σ_{gas} in M51 in $M_{\odot} \text{pc}^{-2}$ derived from the ^{12}CO 2-1 and HI-emission. The cross marks the (0,0) center position at $\alpha = 13^{\text{h}}29^{\text{m}}52^{\text{s}}.7$, $\delta = 47^{\circ}11'43''$ (eq.2000). The $1\text{-}\sigma$ value of the total gas density map is $0.8 M_{\odot} \text{pc}^{-2}$. Contours mark regions discussed in §3.1 and Table 1.

2005. The half power beam width (HPBW) is $11''$. For detailed information of the observations we refer to Paper I.

Additionally, we use data of the HI Nearby Galaxy Survey (THINGS) (Walter et al. 2005, 2008). M51 was observed in the VLA D, C, and B array configurations and presented in Kennicutt et al. (2007). In D-configuration the interferometer is sensitive to scales of $15'$ allowing to detect almost the total flux for M51. The angular resolution in the integrated intensity image is $5.86'' \times 5.56''$. The sensitivity of the THINGS data is $0.44 \text{ mJy beam}^{-1}$ for 5.2 km/s channel width (Walter et al. 2008), which is about a factor 4 deeper than the VLA data of Rots et al. (1990) used in Paper I.

To derive stellar densities, we used the *K*-Band images of the Two Micron All Sky Survey (2MASS) Large Galaxy Atlas (Jarrett et al. 2003).

3. Molecular and atomic gas

3.1. The total gas surface density

In Fig.2 we present a map of the total gas surface density Σ_{gas} . This map is a major ingredient of the gravitational stability analysis we will discuss later in this paper.

To convert from the observed integrated intensities to the total gas surface densities, we use the relation $\Sigma_{\text{gas}} = 1.36 \times (\Sigma_{\text{H}_2} + \Sigma_{\text{H}_1})$ taking into account the mass contribution from He (cf. Paper I). The atomic surface density was calculated from the THINGS HI column density image of M51 (Fig.1), smoothed to $11''$ resolution. Two logarithmic spirals (shown in black) serve as a guide to delineate the inner spiral arms. They are adopted from Shetty et al. (2007) who identified them from a BIMA ^{12}CO 1-0 map of M51.

The total gas surface density in Fig.2 peaks at $127 M_{\odot} \text{pc}^{-2}$. The inner spirals showing the densest peaks just south-west of the center show total gas surface densities of $80\text{-}100 M_{\odot} \text{pc}^{-2}$.

We subdivided the total gas map (Fig.2) into five different regions: the inner and outer spiral arms, the interarm regions, the outer disk, and the companion galaxy. All regions above a threshold surface density of $20 M_{\odot} \text{pc}^{-2}$ were attributed to the spiral arms. The outer border of the outer disk of M51 was defined by the 3σ level of $\sigma_{\text{gas}} = 2.4 M_{\odot} \text{pc}^{-2}$ ($\sigma(\Sigma_{\text{H}_2}) = 0.36 \text{ K km s}^{-1}$, $\sigma(\Sigma_{\text{H}_1}) = 0.44 \text{ K km s}^{-1}$). The threshold for the arms leads to the identification of spiral arms which correspond roughly with the arms seen in interferometric CO maps Shetty et al. (2007), and those seen in $\text{H}\alpha$ -, and in 20 cm radio-continuum emission (Scoville et al. 2001; Patrikeev et al. 2006).

Table 1 lists the average total gas density and the average H_2 over HI density ratio for the five subregions. The average of the inner spiral arm region, is $\Sigma_{\text{gas}} \sim 26.8 M_{\odot} \text{pc}^{-2}$.

The outer spiral arms show less gas surface density, with an average total gas density of $18.8 M_{\odot} \text{pc}^{-2}$, including the south western spiral arm and the north eastern spiral arm. This is approximately a factor of 1.5 weaker than the spiral arms in the central region. Few high density regions on the outer spiral arms reach Σ_{gas} of $40\text{-}50 M_{\odot} \text{pc}^{-2}$ e.g. to the south-west at $(-120'', -200'')$ and the north-east at $(140'', 100'')$. This is significantly weaker compared to the peaks in the center.

Table 1. Properties of Σ_{gas} and $\Sigma_{\text{H}_2}/\Sigma_{\text{H}_1}$ in M51 averaged over the areas shown in Fig.2.

	Σ_{gas} [$M_{\odot} \text{pc}^{-2}$]	$\Sigma_{\text{H}_2}/\Sigma_{\text{H}_1}$
inner spiral arms	26.8	2.3
outer spiral arms	18.8	0.21
interarm region	9.4	0.71
outer disk	6.4	-
NGC 5195 - companion	20.2	0.4
ratio inner/outer spiral	1.4	11.0
inner arm/interarm	2.9	3.2
outer arm/interarm	2.0	0.3

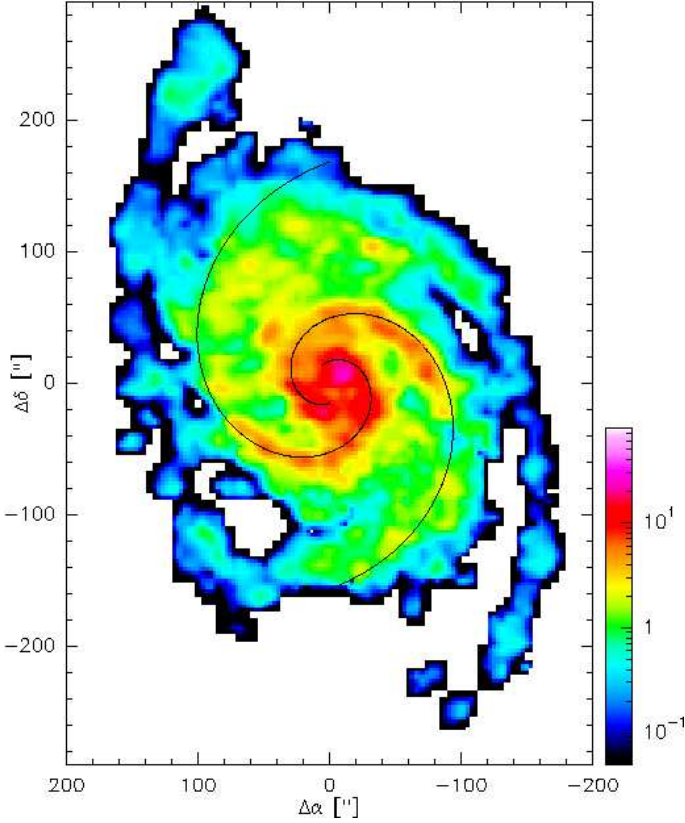


Fig. 3. Map of the ratio of molecular- (Σ_{H_2}) and atomic gas surface density ($\Sigma_{\text{H I}}$) in M51. Pixels below 2σ of the masked-moment integrated intensity image of ^{12}CO 2–1 are blanked. The $1\text{-}\sigma$ limit of the ^{12}CO 2–1 data is 0.65K km s^{-1} corresponding to $\Sigma_{\text{H}_2} = 0.36\text{ M}_\odot\text{ pc}^{-2}$. As the H I is more extended, the threshold of the molecular gas limits the extend of the map.

The interarm regions show surface densities of $5\text{--}15\text{ M}_\odot\text{ pc}^{-2}$. The average value is $9.4\text{ M}_\odot\text{ pc}^{-2}$. The averaged inner arm/interarm contrast in the total gas surface density is 2.9 confirming the results of Garcia-Burillo et al. (1993b) in the integrated CO 2–1 intensities.

There are several spur-like structures bridging the gap between the inner spiral structure and the outer spiral arms e.g. in the north-western area at $(-40'', 80'')$ at a surface density of $20\text{--}30\text{ M}_\odot\text{ pc}^{-2}$. Also, in the north-east at $(100'', 100'')$ there is a strong bridge between inner and outer spiral arms with a total gas surface density of $20\text{--}40\text{ M}_\odot\text{ pc}^{-2}$. The gaps or minima in total gas density seen in the spiral arms e.g. at $(-80'', -40'')$ and at $(-120'', 60'')$ are interpreted as the signature of 4:1 ultra-harmonic resonances by Elmegreen et al. (1989) applying density wave theory.

3.2. The molecular gas fraction

Figure 3 shows the ratio map of molecular versus atomic gas surface density $\Sigma_{\text{H}_2}/\Sigma_{\text{H I}}$. Overall, the map shows a steep decrease of the ratio from peak values of around 50 in the center to 0.1 in the outer regions as already seen in the

radial average (cf. Paper I). The spiral arms in the center are the regions with the highest fraction of molecular gas. The average ratio in the two inner spiral arms delineated in Fig. 2 is 2.1 (Table 1). Outwards, at radii of more than about $100''$, the ratio drops also in the spiral arms. The north-eastern and south-western continuation of the inner spiral arms show few regions with a ratio of 1 or slightly above which are correlated with the regions of increased total gas density (Fig. 2). The average ratio on the outer spiral arms in the marked polygons is 0.21. This is a factor of 10 lower compared to the inner spirals. The interarm region within the inner $100''$ radius shows an average ratio of 0.71. The molecular gas surface density drops below the 2σ threshold at larger radii for most positions.

The increase of the molecular-to-atomic gas fraction in the spiral arms may be triggered by the spiral wave increasing the hydrostatic pressure, and thereby the formation of molecular clouds from the atomic phases of the ISM.

Next, we will discuss the hydrostatic pressure in the disk of M51 as a possible parameter governing the ratio of molecular and atomic gas.

3.3. The hydrostatic pressure

Recent investigations, e.g. by Blitz & Rosolowsky (2004a,b, 2006), have shown a tight correlation of the $\Sigma_{\text{H}_2}/\Sigma_{\text{H I}}$ ratio in external galaxies and the hydrostatic pressure P_{hydro} . Elmegreen (1993) theoretically studied the impact of hydrostatic pressure and radiation field on the ratio of atomic and molecular gas. He concludes that the pressure should be the dominant factor determining this ratio. He predicts a power law $\frac{\Sigma_{\text{H}_2}}{\Sigma_{\text{H I}}} \sim P_{\text{hydro}}^{2.2}$ of their radial averages. Following Blitz & Rosolowsky (2004b), the hydrostatic pressure can be estimated for an infinite disk with isothermal gas and stellar layers from the midplane pressure in equilibrium:

$$P_{\text{hydro}} = (2G)^{0.5} \Sigma_{\text{gas}} \sigma_{\text{gas}} (\rho_*^{0.5} + (\frac{\pi}{4} \rho_{\text{gas}})^{0.5}). \quad (1)$$

Assuming the volume density of the gas ρ_{gas} is small compared to the stellar density ρ_* and a self-gravitating stellar disk ($\Sigma_* = 2\rho_* h_*$):

$$P_{\text{hydro}} = 0.84(G\Sigma_*)^{0.5} \Sigma_{\text{gas}} \frac{\sigma_{\text{gas}}}{h_*^{0.5}}. \quad (2)$$

Σ_* is the stellar surface density, which we will address in a later section, Σ_{gas} the total gas density and σ_{gas} the velocity dispersion of the gas, which we estimated from the ^{12}CO 2–1 velocity dispersion (cf. Paper I). For the stellar scale height, we adopt $h_* = 1\text{ kpc}$, consistent with studies by van der Kruit & Searle (1981); Kregel et al. (2002). P_{hydro} in equation 2 is given in Nm^{-2} , assuming all input parameters are in SI-units.

As in Paper I, radial averages were created by averaging in elliptical annuli spaced by $10''$, including and taking into account points of no detection, and centered at the center position. The annuli are circular rings viewed at an

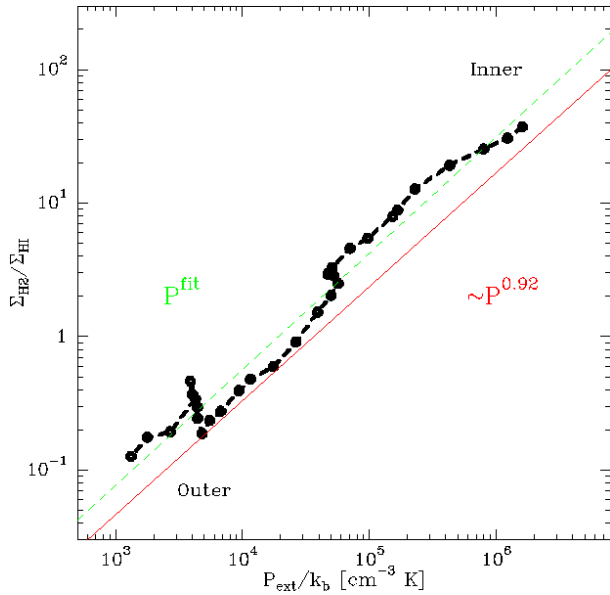


Fig. 4. The radial averaged fraction of molecular gas density Σ_{H_2} and atomic gas density Σ_{H_1} is plotted against the hydrostatic pressure P_{hydro} . The slope found in Blitz & Rosolowsky (2006) is indicated in red. In green the linear regression fit to our data P^{fit} is shown. Going from left to right galactocentric radius decreases.

inclination angle $i = 20^\circ$ and with a line of nodes rotated from north to east by the position angle $\text{PA} = 170^\circ$.

Figure 4 shows the $\Sigma_{\text{H}_2}/\Sigma_{\text{H}_1}$ ratio plotted versus the hydrostatic pressure P_{hydro} , covering three orders of magnitude in pressure, the largest range measured so far in a galaxy disk. A linear regression fit yields a powerlaw:

$$\frac{\Sigma_{\text{H}_2}}{\Sigma_{\text{H}_1}} = (P_{\text{hydro}}/P_0)^\alpha, \quad (3)$$

with the powerlaw coefficient $\alpha = 0.87 \pm 0.03$ and $P_0 = (1.92 \pm 0.07) 10^4 \text{ cm}^{-3} \text{ K}$. The slope of 0.87 is very similar to the slope of 0.92 determined by Blitz & Rosolowsky (2006) for a sample of 14 spiral and dwarf galaxies, including M51. We find a slightly lower P_0 compared to the mean result of Blitz & Rosolowsky (2006) in their sample with $(3.5 \pm 0.6) 10^4 \text{ cm}^{-3} \text{ K}$.

This result underlines the importance of the hydrostatic pressure as the physical parameter determining the fraction of molecular to atomic material at a given radius on large scales. The nearly linear dependence found over the whole pressure regime is expected by theoretical predictions (Blitz & Rosolowsky 2006; Elmegreen 1993), if the gravitational potential imposed by the gaseous component is small compared to the stellar component. Note that the pressure dependence of the molecular to atomic fraction is expected to break down when the spatial resolution of the observational data is close to the size of a single giant molecular cloud (GMC). A single GMC is expected to have enhanced pressure due to self-gravity and the assumption of pressure equilibrium is no longer valid (Blitz & Rosolowsky 2006).

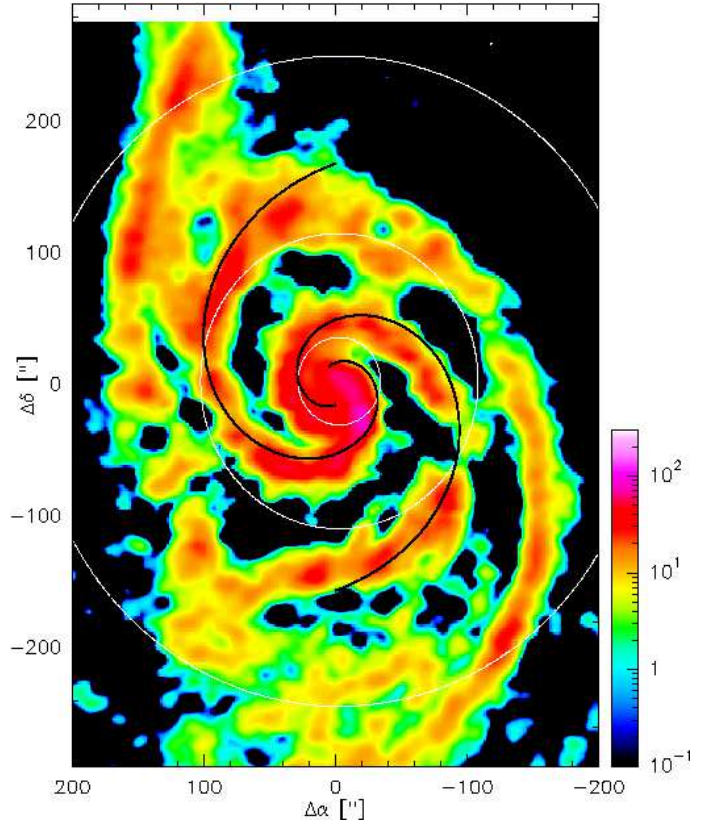


Fig. 5. The residual map of the total gas surface density after removal of a fitted underlying exponential disk. The exponential disk is shown in contours with contour levels $1M_\odot \text{ pc}^{-2}$, $5M_\odot \text{ pc}^{-2}$ increasing to $15M_\odot \text{ pc}^{-2}$ in steps of $5M_\odot \text{ pc}^{-2}$.

3.4. An exponential disk in M51

Table 2. Properties of the exponential disk of the total gas derived in this paper compared to the properties of the exponential dust disk determined by Meijerink et al. (2005).

Total gas exponential disk:	
Σ_{gas} scale length h_{gas}	$7.6 \pm 0.1 \text{ kpc}$
Amplitude: $\Sigma_{\text{gas}}^{\text{peak}}$	$17.8 \pm 0.2 M_\odot \text{ pc}^{-2}$
disk/total mass-fraction gas	61%
Dust exponential disk:	
dust scale length h_{d}	6.3 kpc
Amplitude: $\Sigma_{\text{dust}}^{\text{peak}}$	$0.77 \pm 0.2 M_\odot \text{ pc}^{-2}$
disk/total mass-fraction dust	55%

Next, we investigate the model of an underlying exponential distribution of the total gas density in the disk of M51 and compare it with the dust disk found by Meijerink et al. (2005). We fitted an inclined elliptical exponential disk to the Σ_{gas} total gas surface density distribution map. We assumed a centered disk at an incli-

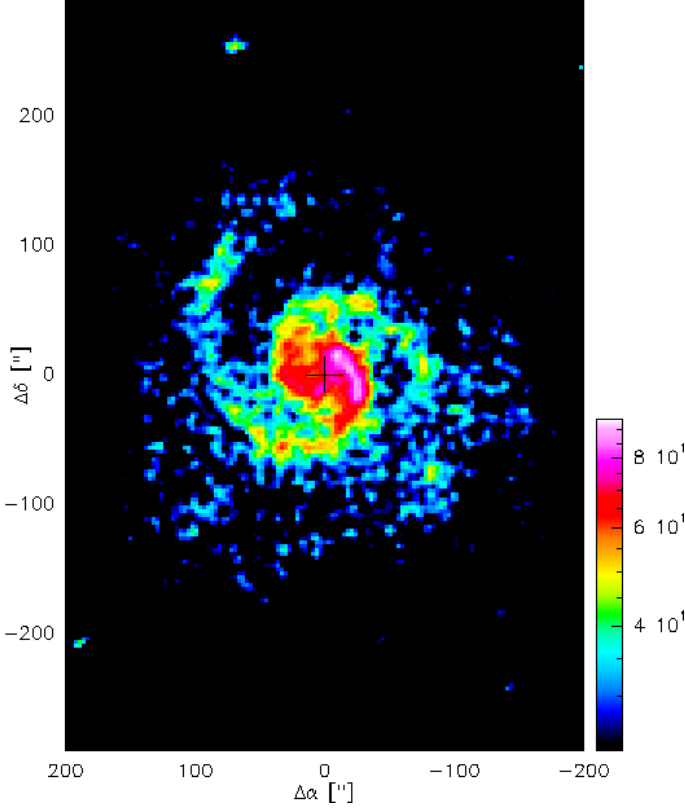


Fig. 6. The residual map of the 850 μ m dust emission after removal of a fitted underlying exponential disk (Fig.2 in Meijerink et al. 2005). The 3 σ -level is at 24 Jy beam $^{-1}$.

nation of 20 $^\circ$ and a position angle of 170 $^\circ$. The scale length h_{gas} and the amplitude $\Sigma_{\text{gas}}^{\text{peak}}$ are determined from a 2-d fit of an exponential distribution $\Sigma_{\text{gas}} = \Sigma_{\text{gas}}^{\text{peak}} \times \exp(-R/h_{\text{gas}})$. All pixels in the total gas density map exceeding a threshold surface density of $\Sigma_{\text{gas}} = 20 \text{ M}_\odot \text{ pc}^{-2}$ were blanked. This corresponds to the arm regions we marked in Fig.2 and discussed in §3.1. A significantly higher blanking threshold leads to an overestimation of the exponential disk in the central parts as spiral arm regions are included in the fitting.

Properties of the exponential disk The scale length of the fitted exponential decay of the total gas disk is $h_{\text{gas}} = 7.6 \text{ kpc}$ (Table 2) with the peak at 17.8 $\text{M}_\odot \text{ pc}^{-2}$. The reduced χ^2 of the fit is 5.1. The fraction of total gas mass contained in the exponential disk is 61%. Thus the spiral arms contain only $\sim 40\%$ of the total gas mass.

Meijerink et al. (2005) fit a scale-length of the exponential dust disk of $h_d = 5.45 \text{ kpc}$ corresponding to $h_d = 6.3 \text{ kpc}$ for a distance of 8.4 Mpc, assumed in the present paper. Assuming an isothermal disk, the fraction of dust contained in the exponential disk is 55%. Notably, the scale lengths of the total gas and of the dust exponential disks are similar, as are the relative fractions of mass contained in the disks.

Note that the shallow radial temperature profile deduced by Meijerink et al. (2005) of 25 K in the center to

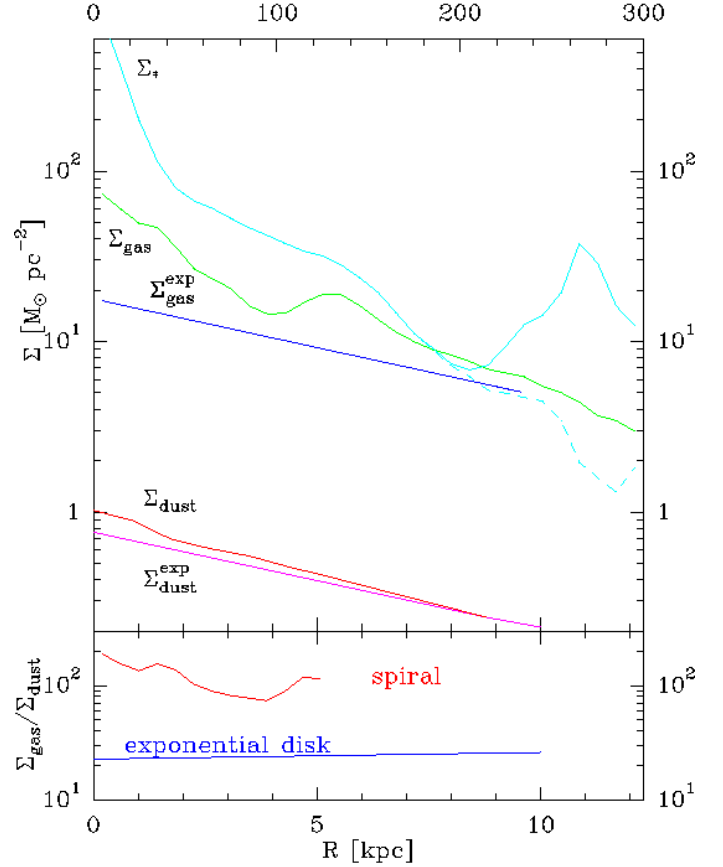


Fig. 7. (a) Radial averages of surface densities. Σ_* is the stellar surface density. Drawn lines show averages including the companion galaxy. The dashed line shows stellar densities, ignoring the companion. Σ_{gas} is the surface density of the total gas. $\Sigma_{\text{gas}}^{\text{exp}}$ is the density of the fitted exponential gas disk. Σ_{dust} is the density of the dusty disk. $\Sigma_{\text{dust}}^{\text{exp}}$ is the density of the exponential dusty disk. Dust values below $3\sigma = 24 \text{ Jy beam}^{-1}$ are ignored. (b) The gas-to-dust ratio for the exponential disk and for the residual data, i.e. the spiral structure.

17 K in the outskirts at 10 kpc radial distance, only leads to a 35% variation of corresponding dust surface densities if the temperature is assumed to be constant. Thus, an isothermal dust disk of 25 K dust temperature and $\kappa_{850} = 1.2 \text{ cm}^2 \text{ g}^{-1}$ (Meijerink et al. 2005) are assumed in the calculation of the dust surface density. The dust surface density Σ_{dust} is

$$\Sigma_{\text{dust}} = M_{\text{dust}}/A_{\text{beam}} = F_{850}d^2/(\kappa_{850}B_{850}(T_{\text{dust}})). \quad (4)$$

$F_{850} = S_{850}/\Omega_{850} \times A_{\text{beam}}$ is the integrated flux. S_{850} is the flux density, Ω_{850} the beam size of 15 $''$ and A_{beam} the beam area at the distance $d=8.4 \text{ Mpc}$. B_{850} labels the Planck-Function at 850 μm .

The radially averaged gas-to-dust mass ratio of the surface densities of the exponential disk is shown in the lower box of Figure 7. The gas-to-dust mass ratio is nearly constant with galacto-centric radius, reflecting the similar scale lengths. Values vary only between 23 and 26, which is

about a quarter of the canonical Galactic gas-to-dust mass ratio of 100. This constancy is in contrast for example to the strong radial variation of the H_2/HI surface density ratio by more than a factor of 100.

The gas-to-dust mass ratio in the exponential disk is significantly lower compared to the canonical Galactic value, whereas the metallicity of M51 is only slightly supersolar with a shallow gradient with varying galactocentric radius (e.g. Kramer et al. 2005). However, several sources of uncertainty enter into this calculation which can not be resolved in the context of this study but might drive the value towards the canonical gas-to-dust mass ratio of 100. In the inner part H_2 dominates the total gas mass and is itself calculated via the X-factor for M51 (see discussion in Paper I). The low gas-to-dust mass ratio in the exponential disk, which constitutes the interarm regions, might indicate an X-factor in the interarm regions closer to the Galactic X-factor (4 times the value of M51). This will on the other hand not severely effect the gas-to-dust mass ratio at larger radii where the atomic component is dominating the molecular contribution.

Additionally, the assumption of a constant dust temperature $T_{\text{dust}} = 25\text{K}$ and $\kappa_{850} = 1.2\text{cm}^2\text{g}^{-1}$ (Meijerink et al. 2005) might cause an overestimation of Σ_{dust} in the exponential disk. A 4 times higher κ_{850} yields a Galactic gas-to-dust mass ratio value but seems unlikely as the values for κ_{850} determined in external galaxies are typically $\kappa_{850} = 0.7 - 2.1\text{cm}^2\text{g}^{-1}$ (James et al. 2002; Alton et al. 2002). A higher dust temperature also drives the gas-to-dust mass ratio towards the Galactic value, with a ratio of 100 for $T_{\text{dust}} = 121\text{K}$ and $\kappa_{850} = 1.2\text{cm}^2\text{g}^{-1}$ as used above.

3.5. Properties of the residual emission

Figures 5 and 6 show the residual total gas and dust maps, after subtracting the corresponding exponential disks. The lower box in Figure 7 shows the corresponding radial averages of the gas-to-dust mass ratio.

For the computation of dust surface density in the residual data, i.e. in the spiral arms, we assume a uniform dust temperature $T_{\text{dust}} = 25\text{K}$ and $\kappa_{850} = 1.2\text{cm}^2\text{g}^{-1}$ (Meijerink et al. 2005) as above.

The resulting fraction of Σ_{gas} and $\Sigma_{\text{dust}}^{\text{can}}$ in the spiral arms, shown in Figure 7, is not constant with radius, but rather varies by almost a factor 3 between about 70 and 190 within the first 5kpc where the emission is above the 3σ -threshold.

In contrast to the gas-to-dust fraction in the exponential disk, we find a minimum of 73 at 3.8 kpc radial distance and a value of 186 in the center. Thus the gas-to-dust mass surface density ratio is a factor of 3-8 higher in the spiral arms compared to the underlying exponential disk.

As the exponential disk constitutes a minor fraction of the gas mass in the spiral arms, it hardly mixes with the spiral arm component.

The global gas-to-dust mass ratio, summing the mass components in the exponential disk and the spiral arms in M51 upto the 3σ -limit of the dust observations, is at 112 close the Galactic value.

4. Stellar surface density

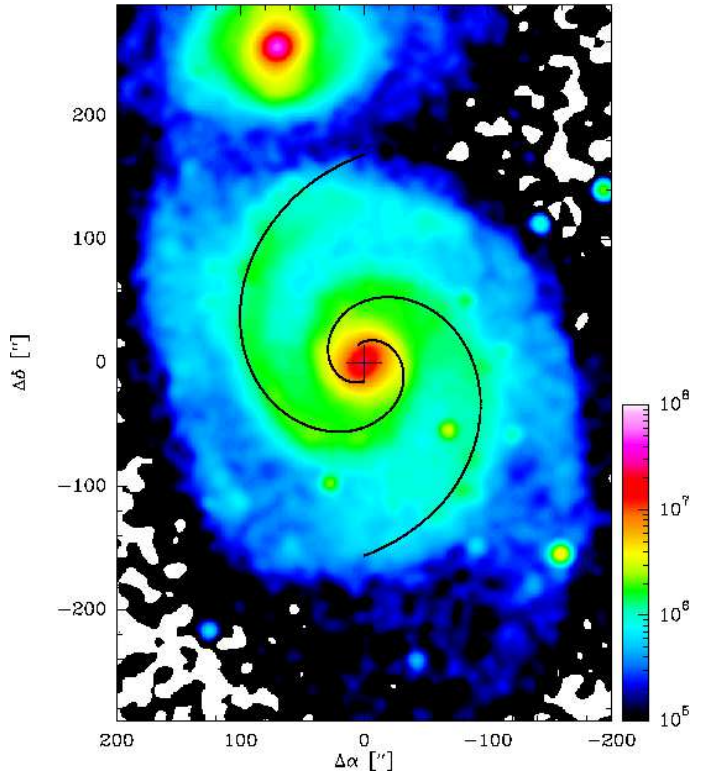


Fig. 8. Map of the K -band luminosity L_K from the Two Micron All Sky Survey (2MASS) Large Galaxy Atlas (Jarrett et al. 2003) smoothed to $11''$ resolution. The units are L_\odot .

The stellar surface density is an important parameter in determining the stability of the disk. We use the K -Band images of the Two Micron All Sky Survey (2MASS) Large Galaxy Atlas (Jarrett et al. 2003) to determine the stellar surface mass density Σ_* . The K -Band is a reasonable tracer of the stellar mass density as it is much less affected by extinction within M51 than e.g. the B -Band in the optical. The Galactic foreground extinction in the K -Band is 0.013 mag compared to 0.152 mag in the B -Band (Schlegel et al. 1998).

Bell & de Jong (2001) discuss mass-to-light ratios in the optical and near-IR passbands. Assuming an universal spiral galaxy initial mass function (IMF), they find variations of the mass-to-light ratio of up to 7 in the optical, 3 in the B -Band and 2 in the K -Band. To convert from luminosities to solar masses, we use a K -Band mass-to-light ratio $M_K/L_K = 0.5 M_\odot/L_\odot$ (Bell & de Jong 2001). The stellar surface density is then determined from the K -Band luminosities via $\Sigma_* = 4.27 \cdot 10^{-5} \times L_K M_\odot \text{pc}^{-2}$ for

a distance of 8.4 Mpc to M51 and an angular resolution of $3''$.

The radial average of the stellar surface density Σ_* is shown in Fig. 7. It decreases from a central value of $\Sigma_* = 810 M_\odot \text{pc}^{-2}$ to $7 M_\odot \text{pc}^{-2}$ before increasing to $12 M_\odot \text{pc}^{-2}$, due to the influence of the neighboring galaxy NGC 5195.

The fraction of stellar-to-gaseous mass density $\Sigma_*/\Sigma_{\text{gas}} = 10.5$ is high in the center, decreasing outwards to values below 1 at a radial distance of about 8 kpc, before increasing again due to NGC 5195.

5. Kinematics of the ^{12}CO 2–1 data

5.1. Velocity field and streaming motions

Figure 9a shows the observed velocity field of the ^{12}CO 2–1 data ranging from 370 to 550 km s^{-1} with the northern part blue-shifted towards us and the southern part of the galaxy red-shifted due to the inclination of the galaxy.

To calculate the velocity field for purely circular motions, we use the rotation curve derived by Garcia-Burillo et al. (1993b,a) and a position angle of $\Theta_{\text{MA}}^{\text{mean}} = 170^\circ$. In addition, we assume a constant inclination of $i = 20^\circ$ and a central velocity of $v_{\text{sys}} = 472 \text{ km s}^{-1}$ (Tully 1974; Shetty et al. 2007). The velocity field at each point in the map is then given by

$$v_{\text{mod}} = v_{\text{sys}} + v(R) \times \cos(\Theta - \Theta_{\text{MA}}^{\text{mean}}) \times \sin(i). \quad (5)$$

with the azimuthal angle Θ . The resulting map is presented in Figure 9b.

The two maps resemble well, i.e. the dominant component creating the observed velocity field is the differential rotation curve $v(R)$ creating the striking X-shape of the iso-velocity contours.

However, the observed velocity field shows in addition many complex structures and distortions not expected from purely rotational motions. We define the residual velocity as the difference of the observed velocity field and purely rotational motions from the rotation curve: $\Delta v_{\text{res}} = v_{\text{obs}} - v_{\text{mod}}$. Figure 10 shows a map of the residual velocities, which we will call streaming motions henceforth.

Streaming motions vary between $\pm 45 \text{ km s}^{-1}$. Strong residual velocities are seen in the center and near the inner spiral arms, e.g. near $(0'', -85'')$ and $(60'', 20'')$. Both outer arms do not show significant streaming motions. We speculate that their locations at radii of $\sim 120 - 170''$ from the galaxy center, lie close to the predicted location of the corotation radius at $160''$ (Garcia-Burillo et al. 1993a,b). At this position no net streaming is expected.

Here, we don't go into more detail, as streaming motions in M51 have previously been discussed by Garcia-Burillo et al. (1993a) using older 30m data and by Aalto et al. (1999) using OVRO data. In addition, Kuno & Nakai (1997) discussed the streaming motions in M51 based on ^{12}CO 1–0 data observed with the NRO 45m telescope. More recently, Shetty et al. (2007) use BIMA

^{12}CO 1–0 data of the entire galaxy at $6''$ resolution to discuss radial and tangential streaming motions in detail. They determined the systemic velocity, position angle, and inclination from a two-dimensional fit to the data.

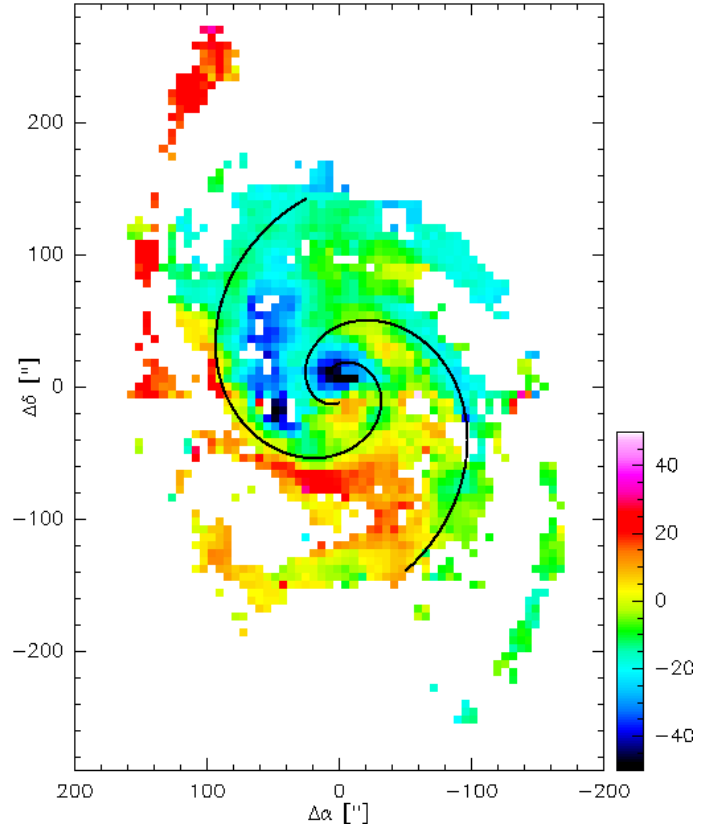


Fig. 10. Map of non-circular streaming motions Δv_{res} , i.e. the deviations of the observed velocity field from circular motions following the rotation curve.

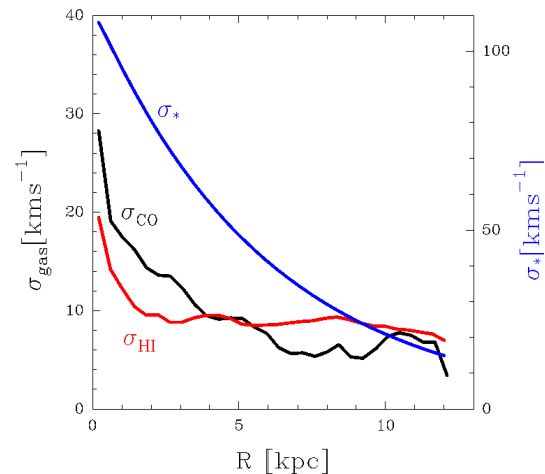


Fig. 12. Radial averages of the velocity dispersions $\sigma = \text{FWHM}/(2\sqrt{2\ln(2)})$ of the molecular gas traced by CO, HI, and stars.

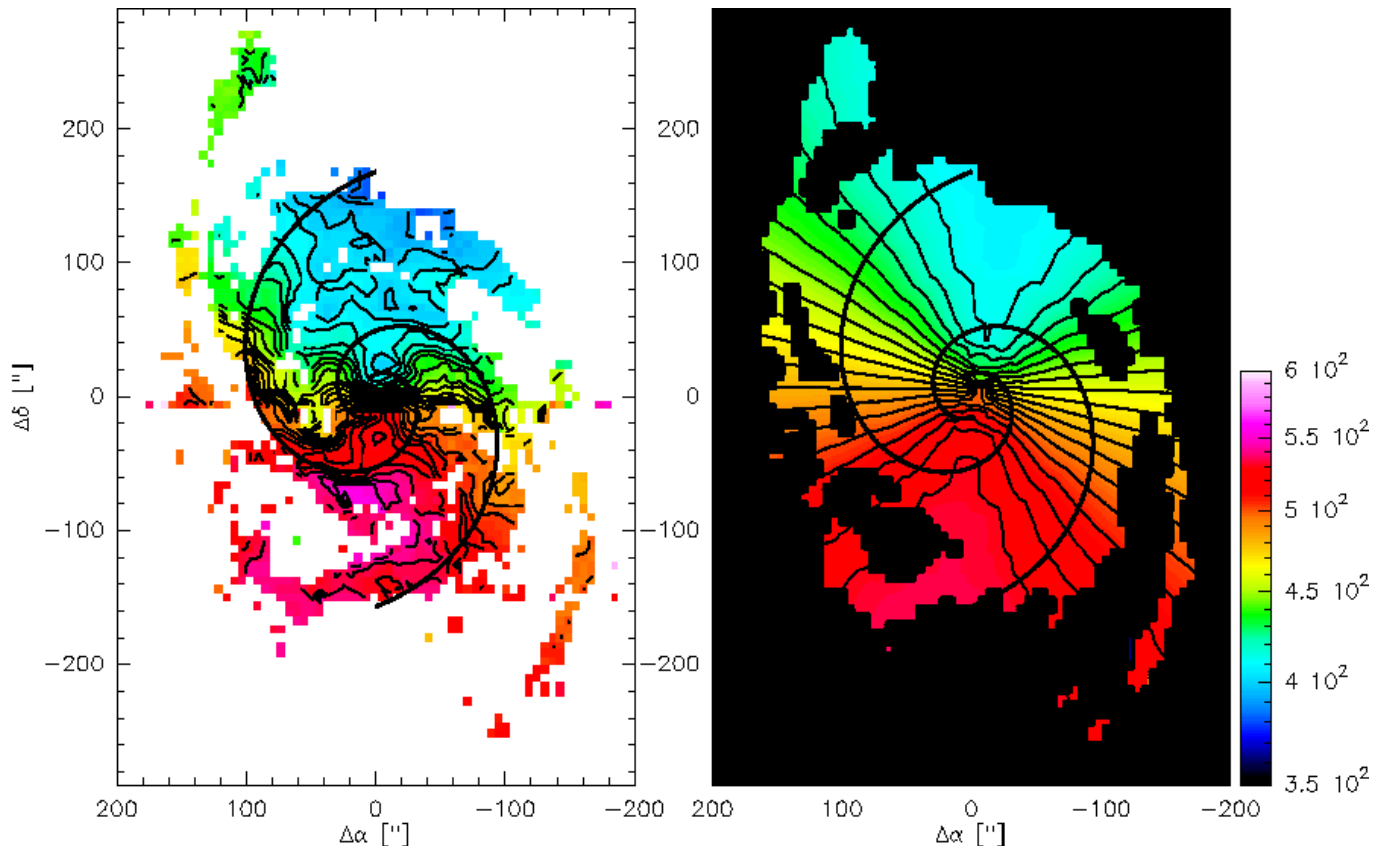


Fig. 9. Left: Map of the first moment $v_{\text{obs}} = \int T v dv / \int T dv$ showing the intensity weighted mean velocity of the ^{12}CO 2–1 data. Data below the 5- σ -level were blanked. **Right:** Map of the calculated velocity field v_{mod} using the rotation curve of Garcia-Burillo et al. (1993b,a). The mean velocities range from 370 to 550 km s^{-1} . Contour levels are in steps of 7 km s^{-1} .

Table 3. Equivalent widths Δv_{eq} of CO and HI in M51 averaged over the areas shown in Fig.2.

	$\Delta v_{\text{eq}}(\text{CO})$ [km s^{-1}]	$\Delta v_{\text{eq}}(\text{HI})$ [km s^{-1}]
inner spiral arms	25.9	21.5
outer spiral arms	11.1	18.3
interarm region	7.3	19.4
ratio inner/outer spiral	2.3	1.2
inner arm/interarm	3.6	1.1
outer arm/interarm	1.5	0.9

5.2. Velocity dispersion of the molecular and the atomic gas

The velocity dispersion of the gas is a signature of the turbulent interstellar medium and systematic motions within the beam. The turbulent medium and the differential rotation curve hinders the medium to collapse under its gravitational pull, as described by the Toomre criterion.

5.2.1. ^{12}CO 2–1

Figure 11a shows a map of equivalent ^{12}CO 2–1 line widths $\Delta v_{\text{eq}} = \int T dv / T_{\text{pk}}$ measuring the velocity dispersion.¹

We will refer to Δv_{eq} in the following as Δv_{obs} the observed line width.

The broadest widths are observed in the center, reaching up to 100 km s^{-1} . In the disk of M51 spiral arms show enhanced line widths relative to the interarm regions. The inner spiral shows strongly enhanced widths relative to the inter arm molecular gas. Along the inner spiral, the widths decrease from about 70 to 20 km s^{-1} . At the same time, the contrast between the arm and interarm dispersion diminishes. Near (60", 100"), arm and interarm molecular gas shows the same dispersion of about 15–20 km s^{-1} . Overall, regions with distances greater than about 100" from the center show significantly lower widths of 15 to 20 km s^{-1} . This drop of CO line widths with radius is also seen in a plot of radial averages (Fig. 12) and in the table of line widths averaged over the inner, the outer, and the interarm regions (Table 3). The outer south-western spiral arm shows uniform widths of around 15 km s^{-1} .

¹ For a Gaussian line profile, the equivalent width corresponds to the full width at half maximum (FWHM).

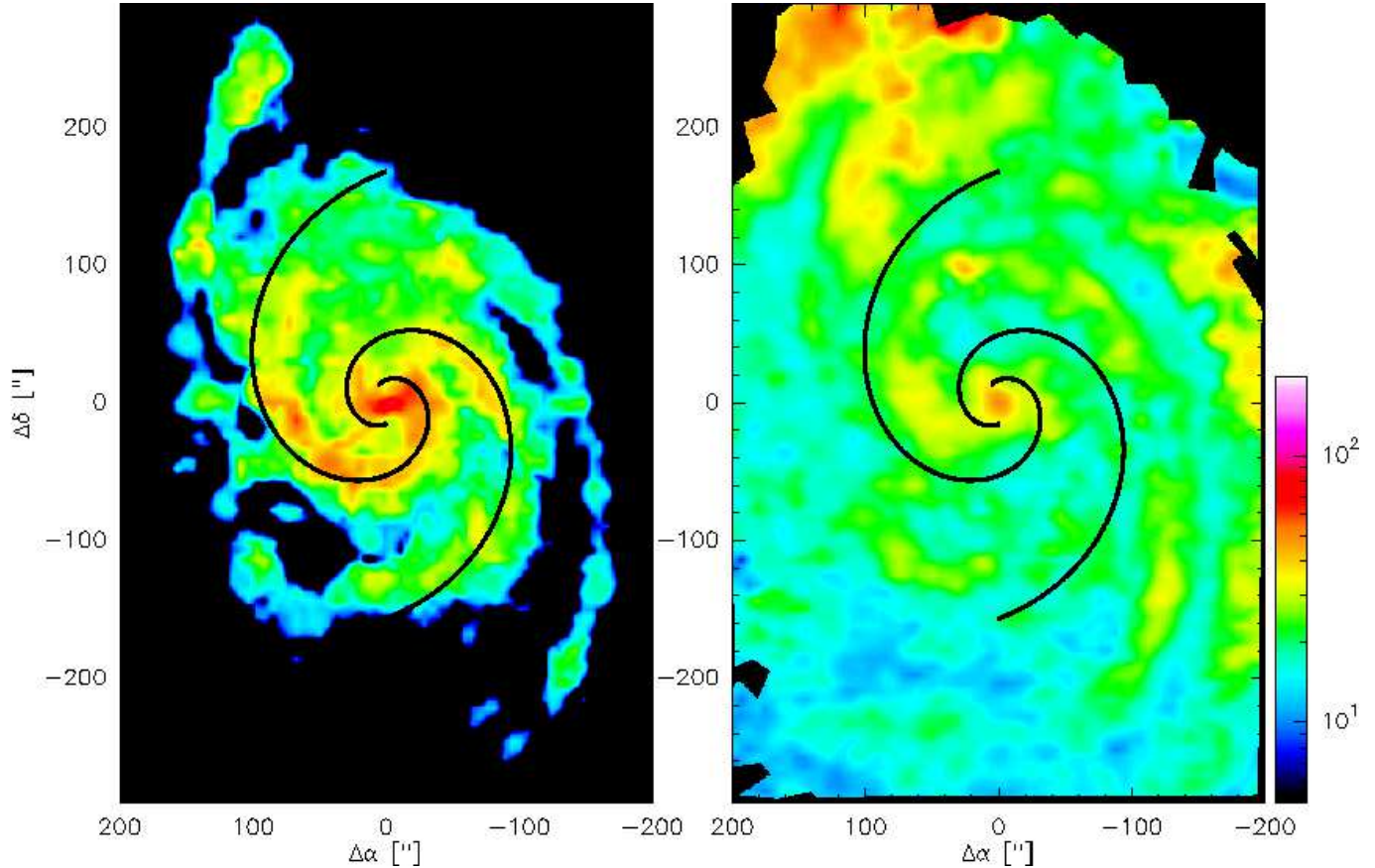


Fig. 11. Velocity dispersions of the molecular and atomic gas in M51. (a) map of observed widths of ^{12}CO 2–1 in km s^{-1} . (b) Velocity dispersion of HI, i.e. map of the square root of the second moment in km s^{-1} . Positions where the HI drops below the 3σ level of $1.33 M_{\odot} \text{pc}^{-2}$ are blanked.

Influence of systemic motions The ^{12}CO 2–1 line widths map in Figure 11a shows no strong systematic broadening of the observed line widths Δv_{obs} with varying angle in the disk which would indicate that a major fraction of the observed line widths originates in the galactic rotation of M51 (modeled in Figure 9b) polluting the observed line widths Δv_{obs} . The velocity gradient within the observing beam (FWHM=11'') due to the velocity field will broaden the observed line widths and thus lead to an overestimation of the intrinsic line width Δv_{obs} . In the following, we will quantitatively estimate the magnitude of this effect on the observed line widths at some selected positions in the galaxy disk where velocity gradients are suspected to be the highest due to projection: the inner region (0''/0'') and along the minor axis. Elsewhere in the disk the gradient of the velocity field is significantly lower (Figure 9b) and additionally the observed line widths are similar to the outer parts of the minor axis (Figure 11a).

Sakamoto (1996) corrected for the broadening due to systemic motions Δv_{sys} using: $\Delta v_{\text{int}}^2 = \Delta v_{\text{obs}}^2 - \Delta v_{\text{sys}}^2$. Δv_{sys} is the velocity variance across the beam as caused by the modeled large scale velocity field. We apply this method to quantify the influence of the rotational motion at the central position (0'',0'') and six other positions

near the minor axis of the galaxy from the center outwards (Figure 13).

The relative error of Δv_{obs} is 12% at the center and decreases outwards along the minor axis with values of less than 3% at distances 90'' away from the center. This relative error is shown together with Δv_{sys} for each of the six studied positions in Figure 13. We estimate the effect of the polluted Δv_{obs} on Q_{tot} (next section) using Gaussian error propagation for a reasonable range of values. The absolute change of Q_{tot} for an overestimation of the line widths of 10% for the gaseous components (the broadening of stellar dispersion due to systemic motions is negligible) results in a maximum absolute uncertainty of 0.16. As this effect is minor, we will in the following neglect the broadening due to rotational motions.

5.2.2. HI

Although line center of CO and HI emission usually coincide quite well, dispersions can be quite different. Figure 11b shows the square root of the second moment $M_2^{1/2} = \sqrt{T v^2 dv / \int T dv}$ of the HI emission as a measure of its velocity dispersion. For a Gaussian line profile, $M_2^{1/2}$ corresponds to the FWHM.

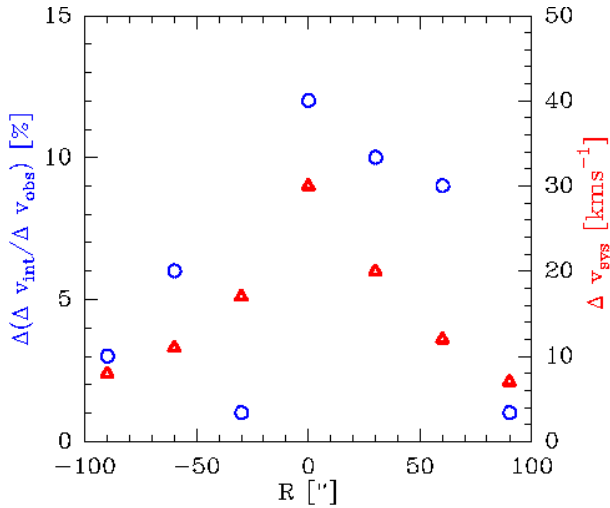


Fig. 13. The overestimation of the intrinsic line widths by the observed line widths near the minor axis $\Delta(\Delta v_{\text{int}}/\Delta v_{\text{obs}})$ in blue circles and the systemic velocity gradient in the beam Δv_{sys} in red triangles for the ^{12}CO 2–1 data.

The HI line widths show values of around 30–50 km s⁻¹ in the central part. In general, the spiral arms do not show up prominently and the interarm regions show a larger dispersion than the spiral arms, in strong contrast to the corresponding CO map. For example, the inner interarm region near (0'', 100'') shows velocity widths reaching values of up to 40 km s⁻¹ which is significantly higher compared to the arm regions. Towards the companion galaxy, we see enhanced widths, comparable to those in the central region. HI shows a strong north-south asymmetry with significantly lower line widths in the southern parts of the galaxy. This is less pronounced in the CO-data. Several of these observations are reflected in the plot of radial averages (Fig. 12) and in the table of line widths averaged over the different regions (Table 3).

In the plot of radially averaged dispersions (Fig. 12), the dispersion of CO gas exceeds the dispersion of HI for radii up to 4 kpc. The decrease of the dispersion of the atomic component in the inner part from around 20 to 10 km s⁻¹ within 2 kpc is steeper compared to the decrease of the CO dispersion. The radial averaged atomic component then stays constant at around 10 km s⁻¹ out to radii of 12 kpc. The CO dispersion drops to 6 km s⁻¹ below the dispersion of HI at radii of around 6 kpc and increases to 11 km s⁻¹ outwards due to the increased dispersion in the center of the companion.

Our findings are consistent with the following scenario (cf. Garcia-Burillo et al. 1993b; Rand et al. 1992). The dispersion of the molecular gas is enhanced in the spiral arms due to frequent collisions of molecular clouds which may be enhanced by streaming motions driven by the density wave. The atomic clouds in the arms appear to form a different population as their local velocity dispersion is much less compared to the molecular gas. We speculate that thus HI in the arms stems mainly from photodis-

sociated H₂ in GMCs, where the dispersion has already decreased due to dissipation. The interpretation of VLA HI and OVRO CO observations by Rand et al. (1992) also favors this dissociation scenario.

The plot of radially averaged dispersions (Fig. 12) also shows the dispersion of disk stars. This is an important parameter for determining the gravitational stability of the disk and will be used in the following section. To estimate the stellar velocity dispersion in M51, we follow Boissier et al. (2003) and Bottema (1993). They showed that the velocity dispersion follows an exponential fall-off $\sigma_{\text{stars}} = \sigma_0 \exp(-R/2h_B)$ depending on the scale length of the B-band h_B of the disk. The B-band scale length is $h_B = 2.82 \text{ kpc}$ (Trewella et al. 2000) and the central stellar velocity dispersion in M51 is $\sigma_0 = 113 \text{ km s}^{-1}$ (McElroy 1995). At radii upto 10 kpc, the velocity dispersion of the stars is larger than that of the molecular and atomic gas components.

6. Gravitational stability

6.1. The combined Toomre parameter Q_{total}

We investigate the gravitational stability of the disk of M51 using the Toomre Q-parameter, taking into account the stellar and gaseous contribution. In general, the Toomre stability criterion is depending on the epicyclic frequency $\kappa(R)$, the velocity dispersion $\sigma(R)$ of the component considered, and the surface density Σ (Toomre 1964), neglecting e.g. the influence of magnetic fields:

$$Q = \frac{\kappa(R)\sigma(R)}{\pi G \Sigma}. \quad (6)$$

The gas should collapse if Q drops below 1, when gravitation dominates over dispersion and the epicyclic frequency.

We treat the molecular gas, the atomic gas, and the stars in the disk of M51 as three independent isothermal fluids using the expansion in wavenumber by Wang & Silk (1994) and neglecting higher order terms in the wavenumber i.e. in the velocity dispersions. The model assumption is that the stars move through the gaseous medium without interaction. For this first order analysis, we assume in addition that the dense molecular clouds move frictionless through the diffuse atomic gas. The total Toomre parameter then is:

$$Q_{\text{tot}}^{-1} = Q_{\text{H}_2}^{-1} + Q_{\text{HI}}^{-1} + Q_{*}^{-1}. \quad (7)$$

For $\kappa(R)$, we use the rotation curve derived from CO, assuming that it holds to the HI gas and for the stars in the disk. For the velocity dispersion $\sigma(R)$, we use the dispersions derived above from CO, HI, and the stars, respectively.

To calculate Q_{*} , we used the 2Mass K-band image smoothed to 11'', as described before. In Fig. 14, the radial averages of Q_{tot} and $Q_{\text{gas}} = (Q_{\text{H}_2}^{-1} + Q_{\text{HI}}^{-1})^{-1}$ are shown.

Taking into account only the HI and CO gas, Q_{gas} drops from values of more than 10 in the center to values

of between 2 and 5 for radii beyond about 1 kpc, as has already been discussed in Paper I. In contrast to Q_{gas} , Q_{tot} is smaller and varies only little between 1.5 and 3, at all radii, staying always close but slightly above the critical value for gravitational instability of 1. This finding indicates a self-regulating disk, keeping the total Toomre Q parameter near 1. We will enter into the discussion of our results in the next section.

The importance of the stellar contribution has also been studied by Boissier et al. (2003), who presented radial averages of the Toomre Q-parameter for their sample of galaxies, comparing Q_{gas} and Q_{tot} . They assume a constant velocity dispersion and find that the stellar contribution lowers the Q-parameter by up to 50% towards the critical threshold. Leroy et al. (2008) very recently also studied the radial averages of the Q-parameter including the stellar contribution in a sample of nearby galaxies from THINGS. They find a marginally stable Q_{tot} in their sample of 23 nearby dwarf and spiral galaxies in accordance with our M51 Q_{tot} -results.

6.2. The influence of streaming motions

Below, we will show that the contribution of non-circular motions to the measured velocity dispersions is small. The influence of streaming motions on the local gravitational stability can therefore be ignored.

To test the influence of non-circular streaming motions on the stability, we correct in the following the observed velocity dispersion for these residual velocities Δv_{res} , assuming Gaussian line profiles:

$$\Delta v_{\text{corr}}^2 = \Delta v_{\text{eq}}^2 - (v_{\text{obs}} - v_{\text{mod}})^2. \quad (8)$$

This reduced dispersion leads to a reduction of Q_{H_2} , assuming that the non-circular streaming motions do not stabilize the gas against collapse.

A local change of the observed line widths Δv_{obs} propagates into Q_{gas} according to Gaussian error propagation. Typical values of $Q_{\text{H}_1} = 1 - 5$, $Q_{\text{H}_2} = 1 - 10$, $\sigma_{\text{CO}} = 10 \text{ km s}^{-1}$ and a variation of 50% of the velocity dispersion, yields absolute variations of Q_{gas} of upto 56% only.

In the radial averages, the maximum relative change between the corrected and uncorrected Q_{tot} is only 7%. In the following, we therefore neglect the streaming motions in the Toomre analysis, and use directly the observed velocity dispersion for the calculation of the Q-parameter.

6.3. The local distribution of Q_{tot}

The local values of the Toomre Q-parameter Q_{tot} at each position are studied in the following. Numerical simulations show that the local Q values can deviate significantly from the radially averaged values. Wada & Norman (1999) use two-dimensional hydrodynamical simulations to study the gravitational stability of the central region of a galactic disk. While global Q-parameter values of their

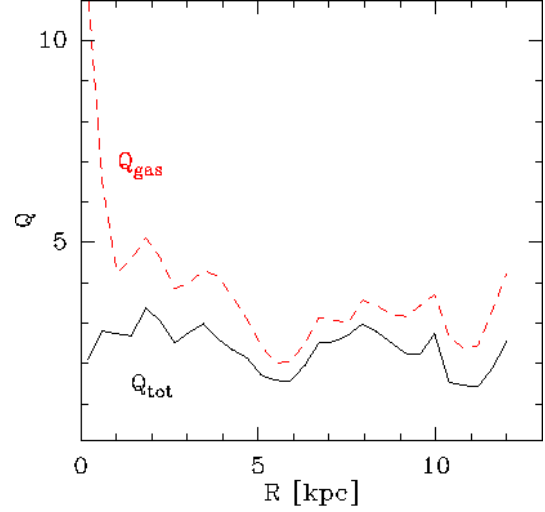


Fig. 14. Radial average of the total Toomre parameter Q_{tot} including the stellar contribution. In red the radial average of the gas-only Toomre parameter Q_{gas} is shown.

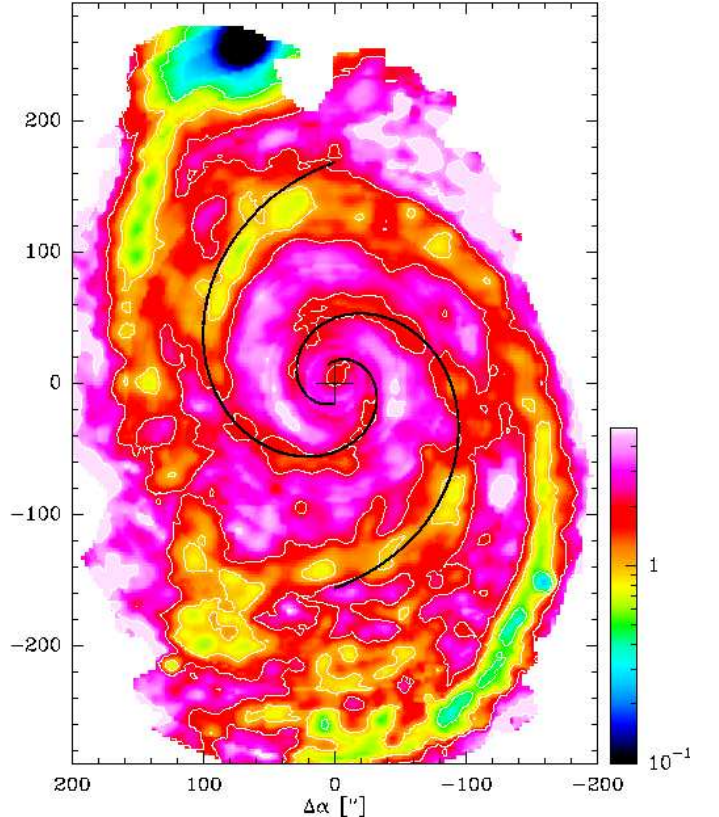


Fig. 15. Map of the total Toomre parameter Q_{tot} including the stellar contribution. We blanked pixels with Σ_{gas} below the 3σ -level. The contours show $Q_{\text{tot}} = 0.5, 1, 2,$ and 5 .

model disk are significantly above the threshold for gravitational collapse, locally the disk shows unstable regions spatially correlated with cold and dense clumps.

Figure 15 shows a map of the Toomre Q-parameter Q_{tot} in M51. In general, spiral arms show smaller values of Q_{tot} , i.e. they are more prone to collapse under the grav-

itational pull, than the surrounding interarm gas. This is expected as star formation occurs predominantly in the spiral arms.

The inner spiral arms show Q_{tot} values between 1 and 2 near to the threshold for gravitational stability. The regions between the inner spiral arms show values up to a factor of 2 to 3 higher as they lack surface density. The outer south-western spiral arm is almost everywhere critical to gravitational collapse with Q_{tot} below 1 or around 1. The outer north-eastern spiral arm shows Q_{tot} of around 1 and below and few small regions reaching values of about 2.

In summary, we see three systematic trends in Q_{tot} : • a slight decrease from the central parts to the outer regions. In the spiral arms, peak values decrease from $\sim 1.5 - 3$ to $\sim 0.5 - 1$. Note that in Paper I no systematic change of the gas depletion times from the inner to the outer parts was found. • Secondly, at a fixed radius, Q_{tot} approaches the regime of instability in the arms, while the interarm regions are stable. • Thirdly, the outer disk beyond the outer spiral arms the disk is stable as well.

A similar study at higher spatial resolution of the total Toomre parameter combining the stellar and gaseous contribution Q_{tot} has been done in the LMC by Yang et al. (2007) using the assumption of a constant velocity dispersion. As the LMC has no prominent spiral structure, the Q_{tot} -map by Yang et al. (2007) also shows no spiral arms with enhanced instability. They also stress the importance of the stellar contribution for studying the gravitational stability. Correlating the locations of massive young stellar objects (YSOs) in the LMC with the gravitational stability, Yang et al. (2007) find that 85% of the YSOs lie inside gravitationally unstable regions. This underlines the importance of gravitational stability of the disk for large-scale star formation in the LMC.

Both galaxies, the LMC and M51, show large regions near the critical value for collapse indicating possible sites for star formation. The observation that Q_{tot} is near 1 in large areas of the disk is notable and was found previously in radial averages of several other galaxies (Boissier et al. 2003). This has led several authors, e.g. Combes (2001), to speculate that self-regulation drives these galaxies near the threshold of gravitational stability.

We will briefly sketch the feedback-cycle in the following. The birthplaces of stars are deeply embedded in dense cores of molecular clouds formed through gravitational contraction and collapse of molecular material after losing much of their turbulent support. Both, bipolar outflows and expanding H II-regions from young stars, stellar winds and supernovae explosions from evolved stars, will introduce mechanical energy into the interstellar medium, locally enhancing the dispersion of the gas, increasing the Q -value. In addition, ionizing radiation from young stars will lead to photo-dissociation of the surface regions and the formation of atomic gas from the molecular material. These feedback mechanisms are supplemented by the density wave, enhancing cloud-cloud collisions due to orbit crowding in spiral arms, also leading to an increase of the

velocity dispersion of the molecular gas inside the arms. Star formation in the remaining molecular gas must await dissipation of the enhanced macroscopic turbulence to cascade down to smaller scales and dissipate. Globally, this self-regulation may explain why Q stays near 1.

In the interarm regions the gas stays stable ($Q_{\text{tot}} > 1$) as no stars are formed and the feedback mechanisms are not at work. The regions critical to collapse in the outer spiral arms coincide with the finding of increased star formation efficiency in these areas by Garcia-Burillo et al. (1993b) based on H α data.

Shetty & Ostriker (2008) use hydrodynamic simulations, including feedback to study star formation and the structure of galactic disks. They find that a simple feedback mechanism with one star formation event per cloud can not sustain a global spiral pattern in galactic disks. This indicates that the modeling of feedback needs to be improved. Quillen & Bland-Hawthorn (2008) explain episodic star formation in galaxies by strong feedback mechanisms using numerical models.

In recent 3D smoothed particle hydrodynamics simulations of isolated disk galaxies, Li et al. (2005, 2006) confirmed the major role of gravitational stability in the process of star formation and were able to examine a threshold surface density. This evidence for the Toomre formalism in their simulations is also dominating any magnetic effects on star formation. Magnetic fields slow the collapse of the gas but do not stop it (Shetty & Ostriker 2008).

7. Summary

Using our complete ^{12}CO 2–1 map of M51 combined with new HI VLA data from the THINGS team (Walter et al. 2005, 2008), we created a total gas density map and a ratio map of molecular and atomic surface density. The total gas density exhibits an underlying exponential disk similar to the one found in 850 μm dust continuum emission by Meijerink et al. (2005). Maps of ^{12}CO 2–1 velocity field, line widths and HI line widths were presented. Combining these information the combined gaseous and stellar Toomre Q -parameter was discussed radially and locally in the disk of M51. The main results of this analysis are:

- The averaged total gas density on the spiral arms is at around $30 M_{\odot} \text{pc}^{-2}$ which is a factor of 3 higher compared to the interarm regions.
- The ratio of molecular to atomic gas surface density is highest in the inner spiral arms at around 50 decreasing to 0.2 in the outer spiral arms. This ratio shows a power-law dependence on the hydrostatic pressure P_{hydro} with an index of 0.87, similar to that found in other nearby galaxies (Blitz & Rosolowsky 2006).
- We fit an underlying exponential disk to the total gas density data with a scale length of 7.6 kpc containing 55% of the total mass. This is comparable to an underlying exponential disk fitted to the 850 μm dust continuum map by (Meijerink et al. 2005). The gas-

- dust ratio in the exponential disk stays nearly constant with galactocentric radius at around 25. The radially averaged map of the gas-to-dust ratio in the residual data shows a variation between 80 and 200.
- The ^{12}CO 2–1 velocity field shows distinct differences with respect to a purely rotational velocity field. We discuss a map of these residual or streaming motions. The observed width of the ^{12}CO 2–1 lines decrease from 100 km s^{-1} in the central part to less than 15 km s^{-1} in the outer regions. The widths of the HI spectra show similar values, but a significantly different distribution. While the CO widths show higher dispersions in the spiral arms, the HI shows the maximum line widths in the interarm regions and lower values on the spiral arms.
 - We estimate the gravitational stability using a combined stellar and gaseous Toomre parameter Q_{tot} . The impact of the stellar component on the stability is significant reducing the Q parameter. It decreases by up to 70% towards the threshold for stability $Q_{\text{total}} = 1$. Q_{total} varies between 5 in the interarm regions decreasing to values below 1 on the spiral arms. In general, the spiral arm regions are closer to the threshold for gravitational instability. The obtained values close to the threshold of 1 indicate self-regulation in the disk of M51. The self-regulation mechanism was discussed on theoretical grounds by (e.g. Combes 2001; Shetty & Ostriker 2008). Similar studies based on extragalactic observations in M83 (Lundgren et al. 2004) or the LMC (Yang et al. 2007) obtained also Q -values close to the threshold for stability.

Acknowledgements. We thank F. Walter for providing us the THINGS VLA HI data and we thank R. Meijerink, R. Tilanus, and F. Israel for providing us the SCUBA $850\ \mu\text{m}$ data of M51. MH acknowledges support from the Bonn-Cologne Graduate School of Physics and Astronomy (BCGS). This work is also financially supported in part by the grant SFB 494 of the Deutsche Forschungsgemeinschaft, the Ministerium für Innovation, Wissenschaft, Forschung und Technologie des Landes Nordrhein-Westfalen and through special grants of the Universität zu Köln and Universität Bonn.

References

- Aalto, S., Huettemeister, S., Scoville, N. Z., & Thaddeus, P. 1999, *ApJ*, 522, 165
- Alton, P. B., Bianchi, S., Richer, J., Pierce-Price, D., & Combes, F. 2002, *A&A*, 388, 446
- Bell, E. F. & de Jong, R. S. 2001, *ApJ*, 550, 212
- Blitz, L. & Rosolowsky, E. 2004a, in *Astronomical Society of the Pacific Conference Series*, Vol. 323, *Star Formation in the Interstellar Medium: In Honor of David Hollenbach*, ed. D. Johnstone, F. C. Adams, D. N. C. Lin, D. A. Neufeld, & E. C. Ostriker, 89
- Blitz, L. & Rosolowsky, E. 2004b, *ApJ*, 612, L29
- Blitz, L. & Rosolowsky, E. 2006, *ApJ*, 650, 933
- Boissier, S., Prantzos, N., Boselli, A., & Gavazzi, G. 2003, *MNRAS*, 346, 1215
- Bottema, R. 1993, *A&A*, 275, 16
- Combes, F. 2001, in *Astronomical Society of the Pacific Conference Series*, Vol. 249, *The Central Kiloparsec of Starbursts and AGN: The La Palma Connection*, ed. J. H. Knapen, J. E. Beckman, I. Shlosman, & T. J. Mahoney, 475
- Elmegreen, B. G. 1993, *ApJ*, 411, 170
- Elmegreen, B. G., Seiden, P. E., & Elmegreen, D. M. 1989, *ApJ*, 343, 602
- Feldmeier, J. J., Ciardullo, R., & Jacoby, G. H. 1997, *ApJ*, 479, 231
- Garcia-Burillo, S., Combes, F., & Gerin, M. 1993a, *A&A*, 274, 148
- Garcia-Burillo, S., Guelin, M., & Cernicharo, J. 1993b, *A&A*, 274, 123
- Heitsch, F., Hartmann, L. W., Slyz, A. D., Devriendt, J. E. G., & Burkert, A. 2008, *ApJ*, 674, 316
- James, A., Dunne, L., Eales, S., & Edmunds, M. G. 2002, *MNRAS*, 335, 753
- Jarrett, T. H., Chester, T., Cutri, R., Schneider, S. E., & Huchra, J. P. 2003, *AJ*, 125, 525
- Kennicutt, Jr., R. C., Calzetti, D., Walter, F., et al. 2007, *ApJ*, 671, 333
- Knapen, J. H., Allen, R. J., Heaton, H. I., Kuno, N., & Nakai, N. 2006, *A&A*, 455, 897
- Kramer, C., Mookerjee, B., Bayet, E., et al. 2005, *A&A*, 441, 961
- Kregel, M., van der Kruit, P. C., & de Grijs, R. 2002, *MNRAS*, 334, 646
- Kuno, N. & Nakai, N. 1997, *PASJ*, 49, 279
- Leroy, A. K., Walter, F., Brinks, E., et al. 2008, *AJ*, 136, 2782
- Li, Y., Mac Low, M.-M., & Klessen, R. S. 2005, *ApJ*, 620, L19
- Li, Y., Mac Low, M.-M., & Klessen, R. S. 2006, *ApJ*, 639, 879
- Lundgren, A. A., Olofsson, H., Wiklund, T., & Rydbeck, G. 2004, *A&A*, 422, 865
- Martin, C. L. & Kennicutt, R. C. 2001, *ApJ*, 555, 301
- McElroy, D. B. 1995, *ApJS*, 100, 105
- Meijerink, R., Tilanus, R. P. J., Dullemond, C. P., Israel, F. P., & van der Werf, P. P. 2005, *A&A*, 430, 427
- Patrikeev, I., Fletcher, A., Stepanov, R., et al. 2006, *A&A*, 458, 441
- Quillen, A. C. & Bland-Hawthorn, J. 2008, *MNRAS*, 386, 2227
- Rand, R. J., Kulkarni, S. R., & Rice, W. 1992, *ApJ*, 390, 66
- Rosolowsky, E., Keto, E., Matsushita, S., & Willner, S. P. 2007, *ApJ*, 661, 830
- Rots, A., Crane, P., Bosma, A., Athanassoula, E., & van der Hulst, J. 1990, *Astronomical Journal*, 100, 387
- Sakamoto, K. 1996, *ApJ*, 471, 173
- Schaye, J. 2004, *ApJ*, 609, 667
- Schlegel, D. J., Finkbeiner, D. P., & Davis, M. 1998, *ApJ*, 500, 525
- Schuster, K. F., Kramer, C., Hitschfeld, M., Garcia-Burillo, S., & Mookerjee, B. 2007, *A&A*, 461, 143

- Scoville, N. Z., Polletta, M., Ewald, S., et al. 2001, *AJ*, 122, 3017
- Shetty, R. & Ostriker, E. C. 2008, *ArXiv e-prints*, 805
- Shetty, R., Vogel, S. N., Ostriker, E. C., & Teuben, P. J. 2007, *ApJ*, 665, 1138
- Toomre, A. 1964, *ApJ*, 139, 1217
- Trewhella, M., Davies, J. I., Alton, P. B., Bianchi, S., & Madore, B. F. 2000, *ApJ*, 543, 153
- Tully, R. B. 1974, *ApJS*, 27, 437
- van der Kruit, P. C. & Searle, L. 1981, *A&A*, 95, 105
- Wada, K. & Norman, C. A. 1999, *ApJ*, 516, L13
- Walter, F., Brinks, E., de Blok, W. J. G., et al. 2008, *ApJ* submitted
- Walter, F., Brinks, E., de Blok, W. J. G., Thornley, M. D., & Kennicutt, R. C. 2005, in *Astronomical Society of the Pacific Conference Series*, Vol. 331, *Extra-Planar Gas*, ed. R. Braun, 269
- Wang, B. & Silk, J. 1994, *ApJ*, 427, 759
- Wong, T. & Blitz, L. 2002, *ApJ*, 569, 157
- Yang, C.-C., Gruendl, R. A., Chu, Y.-H., Mac Low, M.-M., & Fukui, Y. 2007, *ApJ*, 671, 374